Corrosion Behavior of Mild Steel in Sour Environments at Elevated Temperatures

Shujun Gao,[‡,*] Peng Jin,[*] Bruce Brown,[*] David Young,[*] Srdjan Nesic,[*] and Marc Singer[*]

ABSTRACT

The objective of this work was to determine the corrosion rate of mild steel and characterize the corrosion products in sour environments at temperatures ranging from 80°C to 200°C. First, a H_2S–H_2O water chemistry model was developed based on available literature for a closed system at high temperature. Then, H_2S corrosion tests were conducted at 80°C, 120°C, 160°C, and 200°C with an exposure time of 4 d. Linear polarization resistance (LPR) and weight loss (WL) methods were used to measure the corrosion rates. X-ray diffraction (XRD) and scanning electron microscopy with energy dispersive x-ray spectroscopy microanalysis (SEM/EDS) were used to characterize the corrosion products and surface morphology. The results show that the initial corrosion rates increased with temperature then decreased as they achieved steady state. The corrosion product was comprised of two distinct layers. The inner corrosion product was always an iron oxide layer (hypothesized to be Fe_3O_4), while mackinawite, troilite, pyrrhotite, and pyrite were identified as the main components of the outer layer at 80°C, 120°C, 160°C and 200°C, respectively. Pourbaix diagrams generated based on the analysis of water chemistry corroborated the experimental characterization of the corrosion products.

KEY WORDS: hydrogen sulfide, high temperature corrosion, iron sulfide, iron oxide

INTRODUCTION

As geologic environments associated with oil and gas production have become increasingly aggressive, aqueous corrosion at higher temperatures in the presence of hydrogen sulfide (H_2S) is more frequently encountered.[1-3] High temperatures and high pressures in combination with H_2S lead to many materials selection and engineering challenges, as well as potential for pipeline and equipment failures, especially in downhole environments.

H_2S corrosion at low temperatures (<80°C) has been widely studied,[4-6] and significant progress has been made to elucidate the general corrosion mechanisms involved. As a result, kinetic and thermodynamic models have been built and verified. It is known that the initial "bare steel" corrosion rate increases with temperature, but the increase of cathodic current is more significant than that of the anodic current.[7] When conditions are favorable for the formation of a corrosion product layer, its characteristics are strongly dependent on temperature. At 25°C, a porous and non-protective mackinawite layer forms on the steel surface. At 80°C, a dense and adherent corrosion product layer, composed of mackinawite and pyrrhotite, forms that confer good protectiveness.[8] Temperature can accelerate both the rates of corrosion as well as the rate of corrosion product layer formation. Consequently, a peak in corrosion rate is often observed when increasing the temperature at a fixed pH_2S.[9]

At elevated temperatures, sour corrosion has not been investigated thoroughly and the associated

Submitted for publication: December 20, 2016. Revised and accepted: March 22, 2017. Preprint available online: June 8, 2017, http://dx.doi.org/10.5006/2366.

‡ Corresponding author. E-mail: sg389813@ohio.edu.
* Institute for Corrosion and Multiphase Technology, Department of Chemical & Biomolecular Engineering, Ohio University, 342 West State Street, Athens, OH 45701.

ISSN 0010-9312 (print), 1938-159X (online)

corrosion mechanisms are poorly understood. Until now, only a couple papers can be found on the subject in the open literature.[10-11] One was published more than 20 years ago and according to the authors, the corrosion rate at 220°C decreased with time due to iron sulfide growth controlled by direct reaction of H_2S with the metal surface. The corrosion rate eventually reached a stable value due to the balance between layer growth and metal dissolution. Under these conditions, the major corrosion product was identified as pyrrhotite, while traces of pyrite were present. Magnetite was also identified close to the steel surface, but the authors stated that only traces could be detected.[10] Another more recent study identified pyrrhotite at 130°C by characterization using scanning electron microscopy (SEM) and transmission electron microscopy (TEM).[11]

Overall, it is expected that high temperature has a significant effect on:[12-14]

- Corrosion rate.
- Formation of iron sulfide polymorphs and related phases.
- Phase transformations.

Observed phases may also have interactions that lead to surface heterogeneity, onset of galvanic corrosion, and localized attack.

Due to a lack of high-temperature data, both the kinetic and thermodynamic models for sour environments have been verified only up to 80°C.[8,15] In comparison, similar models for CO_2 environments have already been validated for up to 250°C. It has also been reported that magnetite can form at high temperature in CO_2 environments and can significantly slow down the corrosion rate.[16] Whether or not the same is true for H_2S environments is unknown.

Therefore, in order to understand, predict and mitigate H_2S corrosion in oil and gas production at elevated temperatures, further experimental investigations and subsequent construction of new models of H_2S corrosion are a necessity. In this work, a water chemistry model for a H_2S–H_2O system in a closed system at high temperatures was initially developed to better understand the water chemistry and help to properly adjust the relevant parameters in order to achieve the desired environmental conditions at a given temperature. H_2S corrosion tests were then conducted at 80°C, 120°C, 160°C, and 200°C to identify the effect of high temperature on the kinetics of corrosion and layer formation on mild steel in sour environments.

EXPERIMENTAL PROCEDURE

Experiments were performed in a 7-L Hastelloy autoclave, shown in Figure 1. A conventional three-electrode setup was used to conduct linear

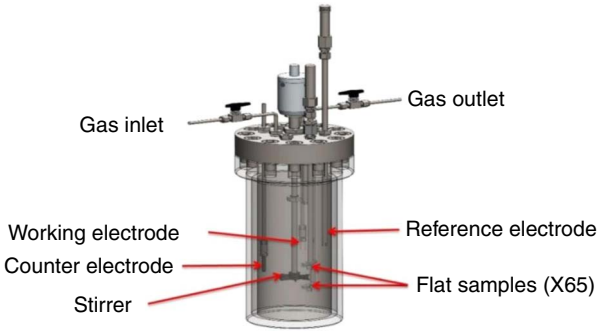

FIGURE 1. *Experimental autoclave setup.*

TABLE 1
Chemical composition of API 5L X65 carbon steel (wt%)

Cr	Mo	S	V	Si	C	P	Ni	Mn	Fe
0.14	0.16	0.009	0.047	0.26	0.13	0.009	0.36	1.16	Balance

polarization resistance (LPR) measurements using a potentiostat. The working electrode was a cylindrical sample made from UNS K03014[1] (API 5L X65) carbon steel, its chemical composition shown in Table 1. A Pt-coated Nb counter electrode and a commercial Zr/ZrO_2 high temperature, high-pressure pH probe was used as a pseudo reference electrode. The pH probe's reference serves as a reference electrode (exact potential still unknown) as long as its potential is stable at the desired test conditions.[16] Four flat $10 \times 10 \times 2$ mm samples were also attached to a stabilized shaft using a PTFE-coated 304SS wire. A centrally located impeller was used to keep the solution fully mixed during each test.

The experimental conditions related to the different tested temperatures were calculated according to the water chemistry model, which will be presented later. A key experimental goal is to start each experiment with a bulk pH of 4.00, once the targeted temperature has been reached. This is achieved by following the experimental procedure outlined below. Some key operating terms are first defined for clarity purposes:

(1) Room temperature conditions:
This is the very starting point of all the experiments at room temperature and pressure, and considering only nitrogen sparging. The pH of the solution is adjusted so that once the target temperature (80°C, 120°C, 160°C, or 200°C) and the target H_2S content (0.00385 mol/L $[H_2S]_{aq}$ at testing temperature) are reached, the solution pH will be 4.00.

(2) Initial conditions:
At this point, all operating conditions (temperature, H_2S content, pH) have been reached. In this study, these initial conditions were pH = 4.00, $[H_2S]_{aq}$ = 0.00385 mol/L at different

[1] UNS numbers are listed in Metals and Alloys in the Unified Numbering System, published by the Society of Automotive Engineers (SAE International) and cosponsored by ASTM International.

temperatures (80°C, 120°C, 160°C, or 200°C). The initial [Fe^{2+}] is assumed to be negligible.

(3) Final conditions:
The final conditions represent the point in time when the experiments were stopped: after 4 d of experimentation, right before the cooling down procedure. The operating conditions at this stage (pH, pH_2S, and [Fe^{2+}]) cannot be measured directly due to technical and safety reasons. However, they are back calculated using measurements performed during the cooling down procedure.

(4) Cooling down conditions:
The system is cooled down to around 50°C to enable H_2S content measurement using gas chromatography. The H_2S is then purged, enabling measurement of pH and [Fe^{2+}] at this temperature. The "cooling down" conditions refer to these measurements. Assuming that [Fe^{2+}] did not change during the cooling down procedure, the parameters corresponding to the "final conditions" (pH and pH_2S) at testing temperature can be calculated.

A H_2S/N_2 gas mixture was injected into the autoclave (no CO_2); the test matrix and experimental details are summarized in Tables 2 and 3.

The following procedure was used in each test:

- the 1 wt% NaCl solution was purged with N_2 overnight at room temperature;
- pH was adjusted to the room temperature condition using a deareated HCl solution (1 M) (see Table 4);
- the API 5L X65 samples were mounted onto the autoclave lid and put into place;
- the electrolyte was further deoxygenated by purging with N_2 for another 1 h (to avoid oxygen contamination during pH adjustment);
- the gas-out valve was closed and N_2 was used to pressurize the system to ensure there were no leaks;
- the system was then depressurized and H_2S was rapidly introduced to the desired pressure (see Table 4);
- the autoclave was then heated up to the desired temperature (initial condition) in a stepwise manner to avoid overheating;
- after reaching the targeted experimental temperature, LPR was conducted between ±5 mV_{OCP} at a scan rate of 0.125 mV/s;
- after 4 d, which was enough to get a relatively stable corrosion rate,[18] the autoclave was cooled to ca. 50°C;
- the H_2S concentration in the gas phase was then measured by gas chromatography (GC);
- N_2 was used to purge the system, and remove remaining H_2S, for ~3 h;
- the autoclave lid was opened (using an H_2S sensor to ensure there was no H_2S remaining) and pH was measured at atmospheric conditions; then the Fe^{2+} concentration of the solution determined using a spectrophotometer;
- the corroded samples were retrieved and characterized by x-ray diffraction (XRD), scanning electron microscopy/energy dispersive x-ray spectroscopy (SEM/EDS), and surface profilometry.

TABLE 2
Test matrix for the effect of temperature

Parameter	Value			
Temperature, °C	80	120	160	200
pH_2S, bar	0.10	0.14	0.17	0.18
Total pressure, bar	8.92	11.89	17.55	28.40
pH	4.00			
$[H_2S]_{aq}$, mol/L	0.00385			
Duration, days	4			

TABLE 3
Experimental details

Parameter	Description
System	7 L Hastelloy autoclave
Solution	1 wt.% NaCl
Specimen	API 5 L X65
Stirring Speed	1000 rpm
Duration	4 days
Measurement Methods	Weight loss, LPR, (Zr/ZrO_2 as a pseudo reference electrode), H_2S concentration (GC)
Surface Characterization	XRD, SEM/EDS, Profilometry

RESULTS

The presentation of the results is divided in two main parts: water chemistry model development and experimental corrosion study at elevated temperature.

Water Chemistry at High Temperatures in a Closed System

Model Construction — In order to define the experimental parameters such as pressure of H_2S and pH in the autoclave, a water chemistry model at high temperatures for a closed (constant inventory) system was developed. The experimental autoclave was identified as a closed system as it was closed after initially purging with gas to a designated pressure. Unlike an open system (typically a purged glass cell), the gas partial pressures in a closed system are not constant; e.g., the H_2S in the gas phase dissolves in water to a given extent depending on temperature and pH, and is not replenished. It is actually extremely difficult to adjust parameters such as solution pH once the system has been pressurized. Instead, a different approach

TABLE 4

Summary of all the experimental conditions (Meas: measured, Cal.: calculated, Asum.: Assumed)

Room Temperature Conditions		Initial Conditions $[H_2S]_{aq}$ = 0.00385 mol/L			Final Conditions			Cooling Temperature Conditions			
pH Meas.	pH_2S, bar Meas.	T, °C	pH Cal.	pH_2S, bar Cal.	pH Cal.	pH_2S, bar Cal.	Fe^{2+}, ppm Asum.	T, °C	pH Meas.	pH_2S, bar Meas.	Fe^{2+}, ppm Meas.
4.04	0.57	80	4.00	0.10	5.47	0.07	1.79	50	6.08	0.47	1.79
4.03	0.52	120	4.00	0.14	5.42	0.11	5.82	54	6.11	0.49	5.82
4.00	0.38	160	4.00	0.14	5.48	0.14	4.26	55	6.23	0.32	4.26
3.97	0.38	200	4.00	0.18	5.78	0.16	2.31	58	6.17	0.35	2.31

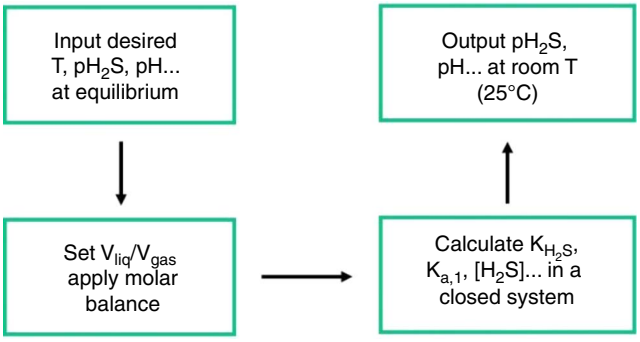

FIGURE 2. *Process of modeling the water chemistry in a closed system at high temperatures.*

was taken, which involves the accurate determination for the corresponding conditions (pH and pH_2S) at ambient temperature and atmospheric conditions, which will lead to the desired conditions once the autoclave is closed and the elevated temperature is reached. The process is shown in Figure 2 and presented described as follows:

- input the desired parameters of T, pH_2S, and pH at equilibrium for the initial conditions (high temperature);
- set the volume ratio between liquid phase and gas phase inside the autoclave;
- use a molar balance for sulfur species in the autoclave; calculate the dissolution and dissociation constants;
- considering a closed system, calculate the corresponding parameters at 25°C and use them as the initial set of conditions.

Care must be taken to select the correct expressions for physical properties and equilibrium constants that are valid at high temperatures. The first important property is the water density, as it experiences considerable changes at high temperatures and will significantly affect the water chemistry. The most widely accepted expression was reported by Jones and Harris:[19]

$$\rho=\frac{999.83952+T_c(16.945176+T_c(-7.9870401\times10^{-3}+T_c(-46.170461\times10^{-6}+T_c(105.56302\times10^{-9}-280.54253\times10^{-12}T_c))))}{1.0+16.87985\times10^{-3}T_c} \quad (1)$$

where ρ is water density in kg/m^3, and T_c is temperature (in °C). This expression was selected to be used in this model because of its widespread adoption, e.g., in the International Temperature Scale (ITS).

The equilibrium constants K_{H_2S}, $K_{a,1}$, and $K_{a,2}$ were calculated based on the research described by Suleimenov, et al.,[20-21] and Ning, et al.[22] [Equations (2)-(10)], but modified from molality to molarity units. Originally, these values were as molality units (mol/kg bar), but were here used in molarity (mol/L bar) as the numerical values are very close at temperatures under 100°C.[7,22] However, as shown in Figure 3, when used at higher temperature (typically above 100°C), large differences can appear (e.g., more than 25% error is apparent at 250°C):

$$H_2S(g) \overset{K_{H_2S}}{\Leftrightarrow} H_2S(aq) \quad (2)$$

$$K_{H_2S}=\frac{[H_2S]}{p_{H_2S}} \quad (3)$$

$$K_{H_2S}=10^{-(634.27+0.2709T_K-0.00011132T_K^2-16719/T_K-261.9\log T_K)} \quad (4)$$

$$H_2S(aq) \overset{K_{a,1}}{\Leftrightarrow} H^+(aq)+HS^-(aq) \quad (5)$$

$$K_{a,1}=\frac{[H^+][HS^-]}{[H_2S]} \quad (6)$$

$$K_{a,1}=10^{782.43945+0.361261T_K-1.6722\times10^{-4}T_K^2-20565.7315/T_K-142.741222\ln T_K} \quad (7)$$

$$HS^-(aq) \overset{K_{a,2}}{\Leftrightarrow} H^+(aq)+S^{2-}(aq) \quad (8)$$

$$K_{a,2}=\frac{[H^+][S^{2-}]}{[HS^{-1}]} \quad (9)$$

$$K_{a,2}=10^{-(23.93-0.030446T_K+2.4831\times10^{-5}T_K^2)}. \quad (10)$$

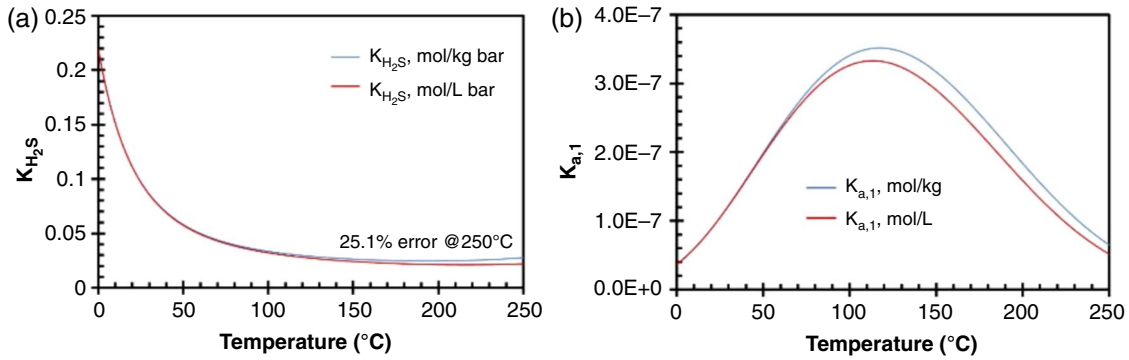

FIGURE 3. *(a) K_{H2S} and (b) $K_{a,1}$ values with respect to molality and molarity at different temperatures.*

Parametric Study — A parametric study was completed to predict the calculated variation of species concentrations at different temperatures. This was an essential step in properly designing any experimental conditions. The effect of V_{liq}/V_{gas} ratio on the water chemistry is shown in Figure 4. Being able to anticipate and understand the effect of this ratio is important as, ideally, the test conditions should simulate an open system where the partial pressure of H_2S is constant. This is not possible in an autoclave setup but the characteristics of an open system can be closely approached if the right conditions are selected. Figure 4 shows that the behaviors of $[H_2S]_{aq}$, $[HS^-]$, and $[S^{2-}]$ concentrations are different in an open and closed system at higher pH values. The discrepancy is more apparent at a higher liquid/gas volume ratio (i.e., a large volume of liquid). The total amount of H_2S (sum of all the sulfide species) that needs to be injected into the 7-L autoclave increases with decreasing gas volume for a fixed H_2S partial pressure and pH 4.00. On the other hand, choosing a low liquid volume would lead to rapid change in chemistry due to the generation of corrosion products. At a V_{liq}/V_{gas} ratio of 6, the discrepancy between open and closed systems is minimized. This ratio is therefore chosen in this work for every experimental temperature.

The effect of temperature on the concentrations of sulfide species at a fixed pH 4.00 and 0.10 bar pressure of H_2S is shown in Figure 5(a). All of the species concentrations significantly vary with increasing temperature. However, what really matters for corrosion is not pH_2S, but the concentration of dissolved H_2S in the solution, $[H_2S]_{aq}$. In this work, $[H_2S]_{aq}$ was kept at 0.00385 mol/L for every temperature to enable better comparisons. This corresponds to 0.10 bar H_2S at 80°C. In order to maintain $[H_2S]_{aq}$ as a constant at higher temperatures, the pH_2S needs to be increased (Figure 5[b]). H_2S corrosion at 80°C, 120°C, 160°C, and 200°C at a constant $[H_2S]_{aq}$ will be investigated in this work.

Experimentally, the water chemistry at high temperature should be monitored and compared with theoretical values. Currently, due to the lack of a reliable reference electrode in high temperature and high-pressure H_2S environments, pH could not be measured in situ. However, the chemistry is calculated considering literature data (ρ, K_{H2S}, $K_{a,1}$, and $K_{a,2}$) that have been verified up to 250°C.[19-21] Therefore, the water chemistry verification could not be directly

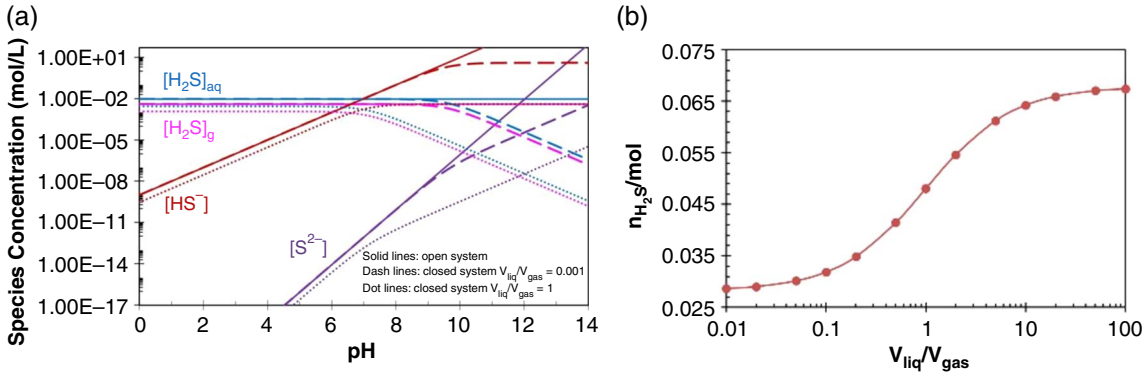

FIGURE 4. *(a) Effect of V_{liq}/V_{gas} ratio on the concentrations of sulfur species, and (b) the total amount of H_2S in a 7-L autoclave at pH 4.00, T = 25°C, pH_2S = 0.10 bar.*

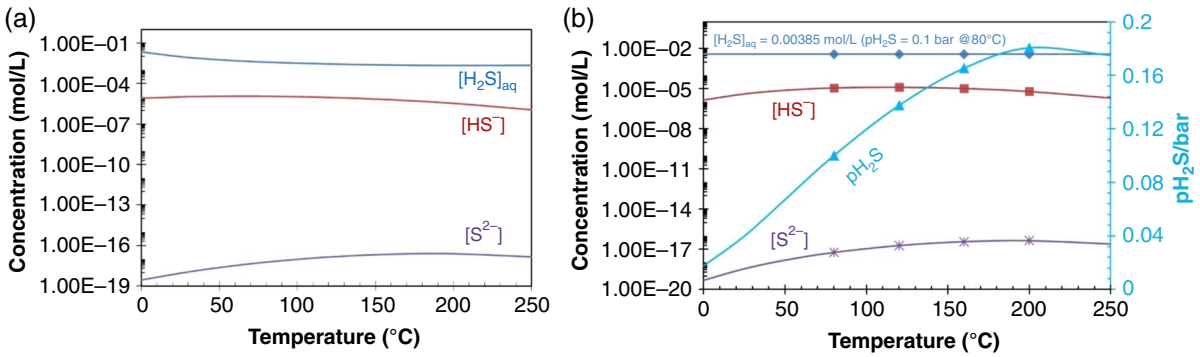

FIGURE 5. *Effect of temperature on concentrations of sulfur species at (a) constant $pH_2S = 0.10$ bar and (b) constant $[H_2S]_{aq} = 0.00385$ mol/L ($pH_2S = 0.10$ bar at 80°C), pH = 4.00.*

done, but had to be back-calculated by characterization of liquid samples taken at the end of each experiment.

Effect of High Temperature on H_2S Corrosion

Experiments based on the test matrix in Table 2 were performed to identify the effect of high temperature on the kinetics of corrosion and layer formation on mild steel in sour environments. The results are presented below.

Corrosion Rates — Figure 6 shows the corrosion rates over time at 80°C, 120°C, 160°C, and 200°C as measured by LPR. It can be seen that the initial corrosion rates increased with increasing temperature, and then quickly decreased to stable corrosion rates of 4.1 mm/y, 3.8 mm/y, 1.8 mm/y, and 2.5 mm/y, respectively, from lowest to highest temperature. Overall, the steady-state corrosion rate decreased with temperature except at 200°C.

The time-averaged corrosion rates obtained from weight loss are shown in Figure 7. They are in good agreement with the time-integrated corrosion rate from LPR using a B value of 23 mV/decade.

Corrosion Products — The corrosion products on the steel surface were characterized by XRD as shown in Figure 8. While mackinawite (FeS) was the main

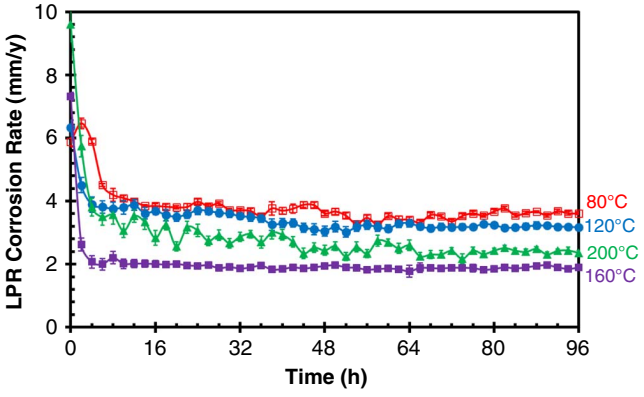

FIGURE 6. *Corrosion rate at different temperatures from LPR measurement, $[H_2S]_{aq} = 0.00385$ mol/L, pH = 4.00, 4 d, B = 23 mV/decade.*

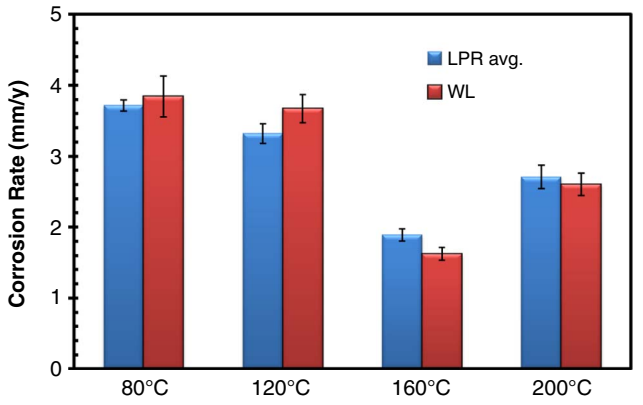

FIGURE 7. *Comparison of corrosion rates between LPR and weight loss, $[H_2S]_{aq} = 0.00385$ mol/L, pH = 4.00, 4 d, B = 23 mV/decade.*

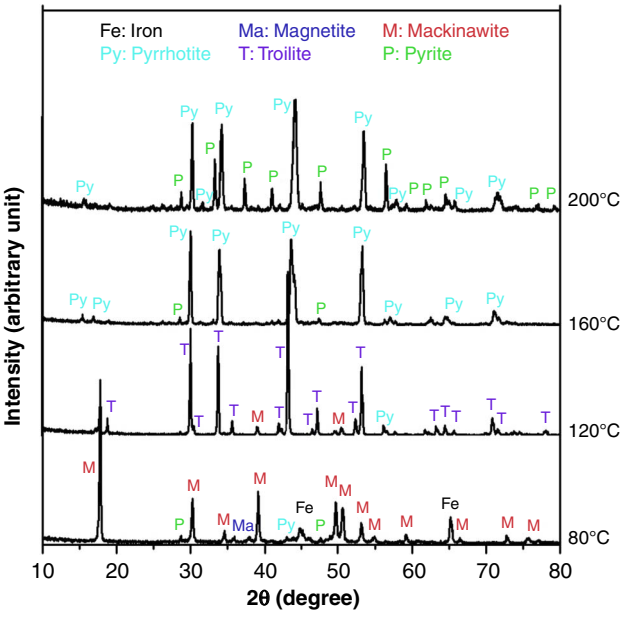

FIGURE 8. *XRD patterns of corrosion products on the steel surface at different temperatures, $[H_2S]_{aq} = 0.00385$ mol/L, pH = 4.00, 4 d.*

corrosion product detected at 80°C, troilite (FeS), pyrrhotite ($Fe_{1-x}S$, x = 0–0.17) and pyrrhotite/pyrite (FeS_2) became the dominant species as temperature was increased. With increasing temperature, the corrosion product became richer in sulfur; this is an indication of enhanced reaction kinetics for phase transformations.

The morphologies of the formed corrosion products were also characterized by SEM, as shown in Figures 9 and 10. The SEM for the 80°C specimen shows a mackinawite layer of 15-µm thickness, which is much thinner than the corresponding metal loss thickness calculated to be 42 µm. From the EDS line scan, the outer layer was identified to be likely an iron sulfide but an inner layer, which consisted mostly of iron and oxygen was probably an iron oxide. At 120°C, the SEM shows troilite-like crystals on the surface and a much thicker layer (61 µm–73 µm). The α-Fe peaks are absent in the XRD pattern as the corrosion product is so thick, preventing the x-rays from reaching the metal substrate. At 160°C, pyrrhotite crystals were clearly observed. The thickness of the layer was only about 10 µm, but still no α-Fe peaks were detected by XRD, indicating the corrosion product layer was very dense and compact. This is also probably why the corrosion rate at 160°C was the lowest. The corrosion products changed to planar flaky crystals at 200°C. All of the cross sections show a two-layer structure at every temperature tested: an inner layer comprised of an iron oxide and an outer

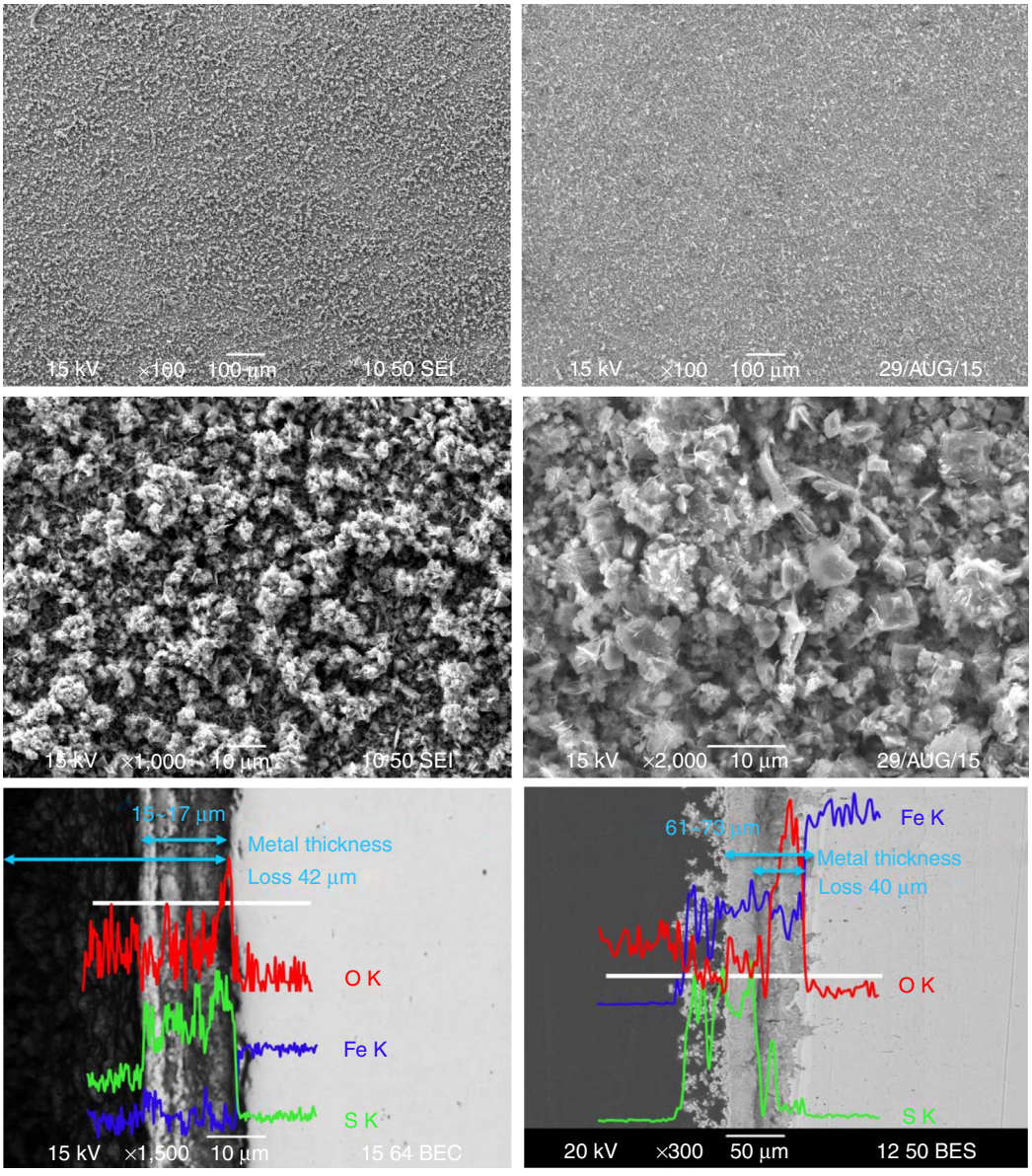

FIGURE 9. *SEM of morphologies and cross-sections at 80°C (left) and 120°C (right), $[H_2S]_{aq}$ = 0.00385 mol/L, pH = 4.00, 4 d.*

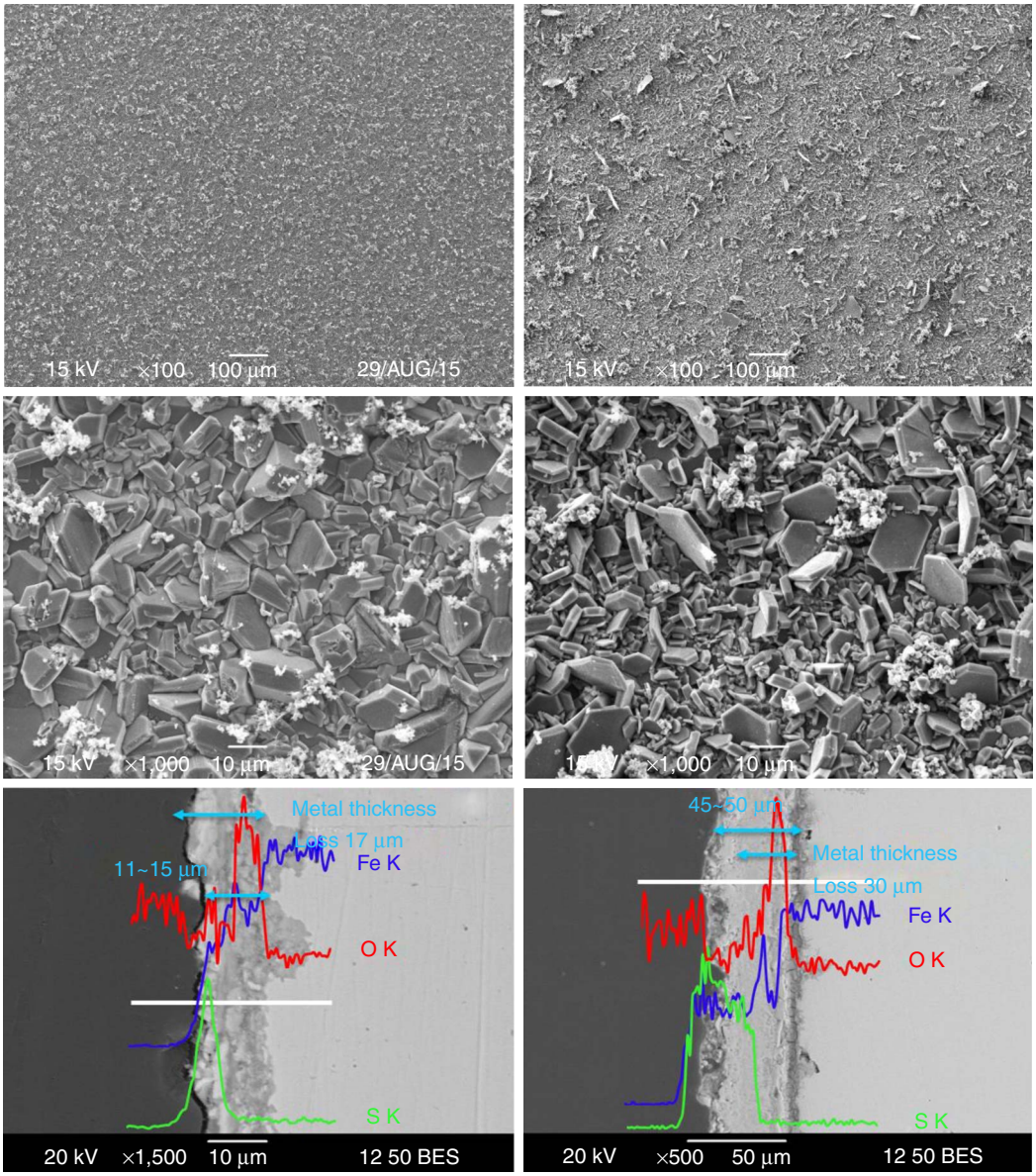

FIGURE 10. *SEM of morphologies and cross-sections at 160°C (left) and 200°C (right), $[H_2S]_{aq}$ = 0.00385 mol/L, pH = 4.00, 4 d.*

layer comprised of an iron sulfide. However, the iron oxide was not detected by XRD due to the top layer being too thick and compact for XRD penetration.

Surface Profilometry — After removal of the corrosion products using Clarke solution,[23] the metal surface was characterized by profilometry, as shown in Figures 11 and 12. No obvious localized corrosion was observed at 80°C and 120°C. The surface was relatively smooth and the corrosion could be considered as uniform. However, at 160°C some small pits could be observed with around a 1.2 pitting ratio (ratio of maximum pit rate to general corrosion rate) and 1.5 mm/y pit penetration rate. This can be treated only as localized corrosion initiation. At 200°C, many large pits appeared with a 3.2 pitting ratio and 8.2 mm/y pit penetration rate. The pitting ratio is not accurate as the pitting corrosion overwhelmed the whole general corrosion. Due to severe localized corrosion at this temperature, the stable LPR corrosion rate was a little higher than at 160°C (Figure 6). These results fit with Ning's previous work[24] where it was found that once there is pyrite formation, localized attack would occur.

DISCUSSION

The current results are insufficient to make conclusive mechanistic statements; however, there are some new findings that are worthy of a discussion, especially in the context of the existing literature.

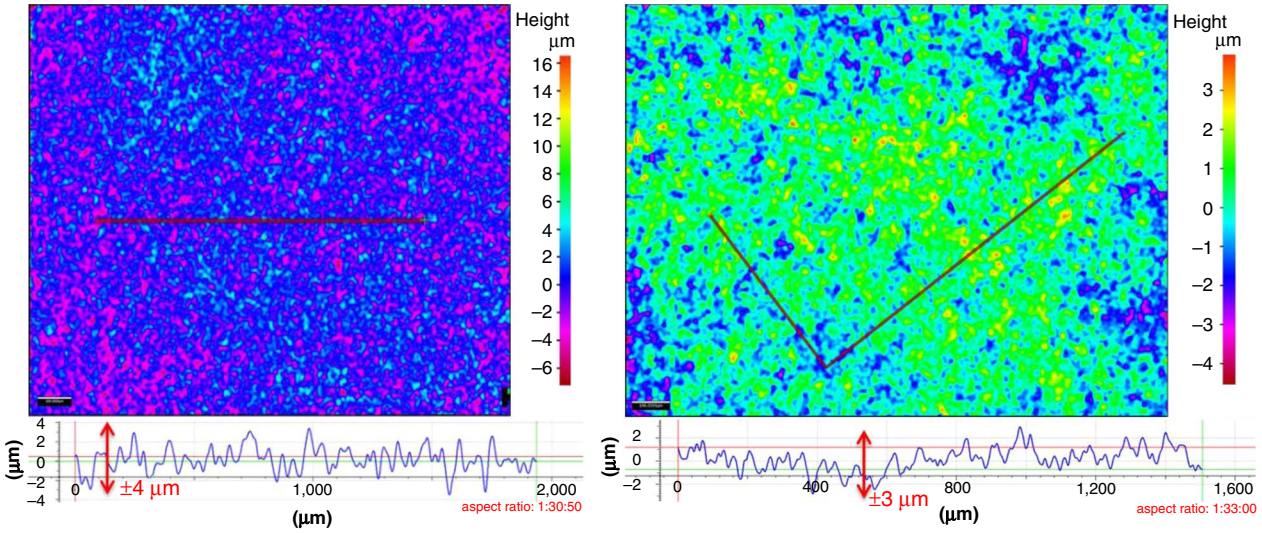

FIGURE 11. *Surface profilometry after removing corrosion products at 80°C (left) and 120°C (right), $[H_2S]_{aq}$ = 0.00385 mol/L, pH = 4.00, 4 d.*

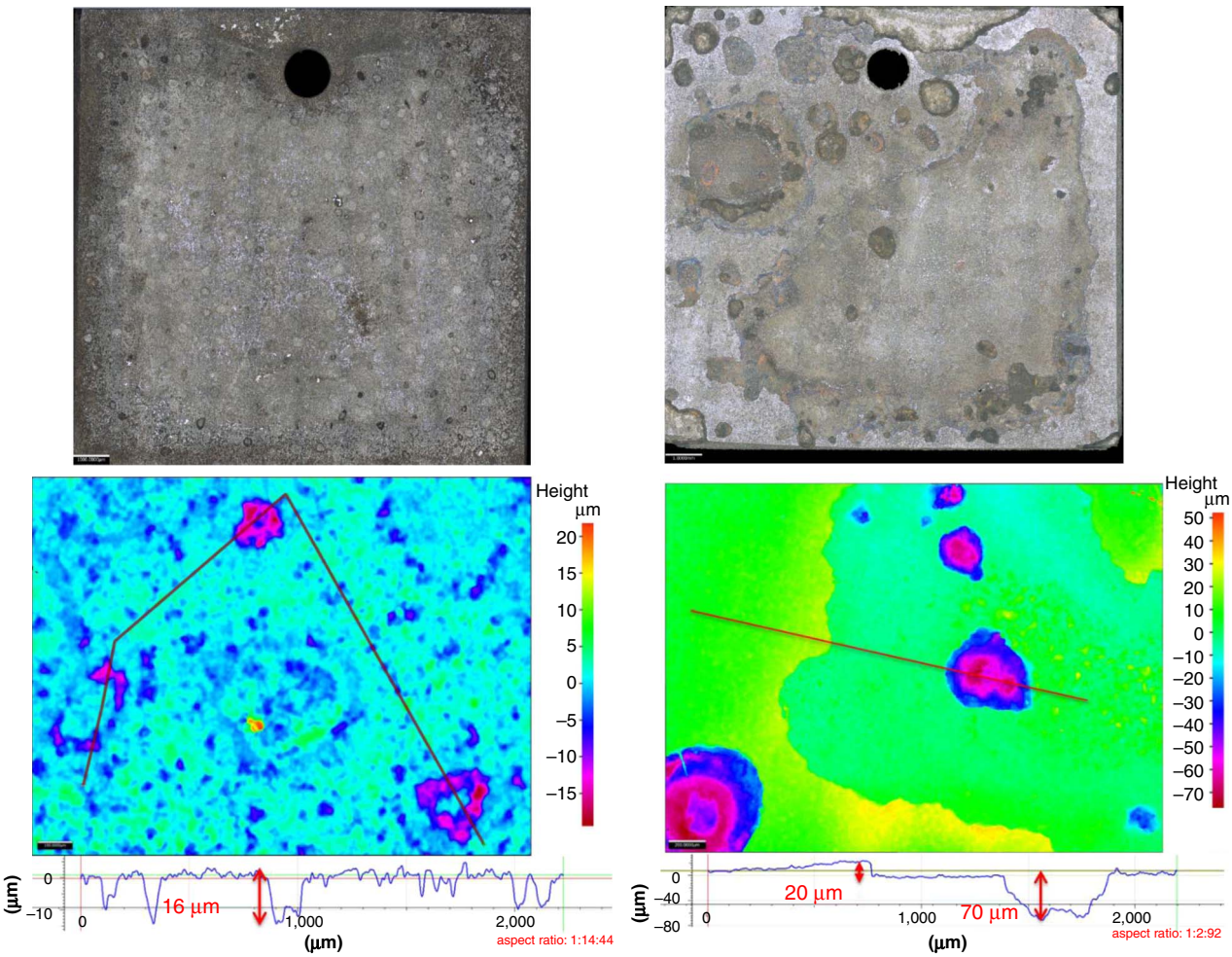

FIGURE 12. *Surface profilometry after removing corrosion products at 160°C (left) and 200°C (right), $[H_2S]_{aq}$ = 0.00385 mol/L, pH = 4.00, 4 d.*

Formation of Iron Oxide

Iron oxide was found, at every temperature tested, as the main component of the inner corrosion product layer (Figures 9 and 10). Until now, iron oxide has not been given much attention as a corrosion product in H_2S corrosion environments. It is hypothesized that this iron oxide is magnetite (Fe_3O_4) due to the following observations:

- two Fe_3O_4 peaks were observed from XRD analysis at 80°C (Figure 8), though they were not detected at other temperatures due to the top layer being either too thick or too compact for x-ray penetration;
- Fe_3O_4 was also confirmed as an inner layer from a previous study in sour environments at 220°C;[10]
- Fe_3O_4 is also the main corrosion product at high temperatures in CO_2 environments.[16]

The kinetics of Fe_3O_4 formation is very fast, making the scaling tendency (ST that is the ratio of precipitation rate to corrosion rate) very high at high temperature. Fe_3O_4 can form on the metal surface according to reaction (11):

$$3Fe^{2+}(aq) + 4H_2O(l) \Leftrightarrow Fe_3O_4(s) + 8H^+(aq) + 2e^-. \quad (11)$$

From the Pourbaix diagram shown in Figure 13, considering a sweet (CO_2 dominated) system, Fe_3O_4 is dominant in a very limited narrow area at potentials more positive than those for $FeCO_3$ at 80°C. When the temperature increases to 200°C, the possibility for Fe_3O_4 of being the dominant species is greatly increased. Similarly, in sour corrosion at high temperature, the iron oxides should be taken into account, along with the iron sulfides.

Formation of Iron Sulfide

The objective of this section is to compare the thermodynamic predictions for the formation of corrosion products with the experimental results.

The thermodynamic prediction model is based on Ning's work,[8] which has not been verified above 80°C. In order to do so, a good understanding of the water chemistry at operating conditions needed to be developed. As no direct measurement of pH and Fe^{2+} concentration could be performed in situ, some assumptions are needed as described below.

The H_2S concentration and Fe^{2+} concentration were measured using GC and spectrophotometry, respectively, after cooling down the autoclave (usually to around 50°C). The water chemistry was calculated at this measured temperature according to Equations (3), (6), (9), (13), and (15):

$$H_2O(l) \overset{K_w}{\Leftrightarrow} H^+(aq) + OH^-(aq) \quad (12)$$

$$K_w = [H^+][OH^-] \quad (13)$$

$$K_w = 10^{-(29.3868 - 0.0737549 T_K + 7.47881 \times 10^{-5} T_K^2)} \quad (14)$$

$$[Na^+] + 2[Fe^{2+}] + [H^+] = [Cl^-] + [HS^-] + 2[S^{2-}] + [OH^-]. \quad (15)$$

In Equation (15), for determining electroneutrality, the $[Cl^-]$ is known experimentally by recording how much NaCl and HCl (for pH adjustment) were added. There are five equations and five unknowns ($[H_2S]$, $[HS^-]$, $[S^{2-}]$, $[H^+]$, and $[OH^-]$). The total amount of sulfur species was calculated by applying a molar balance:

$$\sum S = [H_2S]_g + [H_2S]_{aq} + [HS^-]_{aq} + [S^{2-}]_{aq} = \text{constant}. \quad (16)$$

It is assumed that no significant gain or loss of Fe^{2+} occurred during the test "cooling down" procedure, either by FeS precipitation or dissolution. The $[Fe^{2+}]$ concentration measured at the sampling temperature

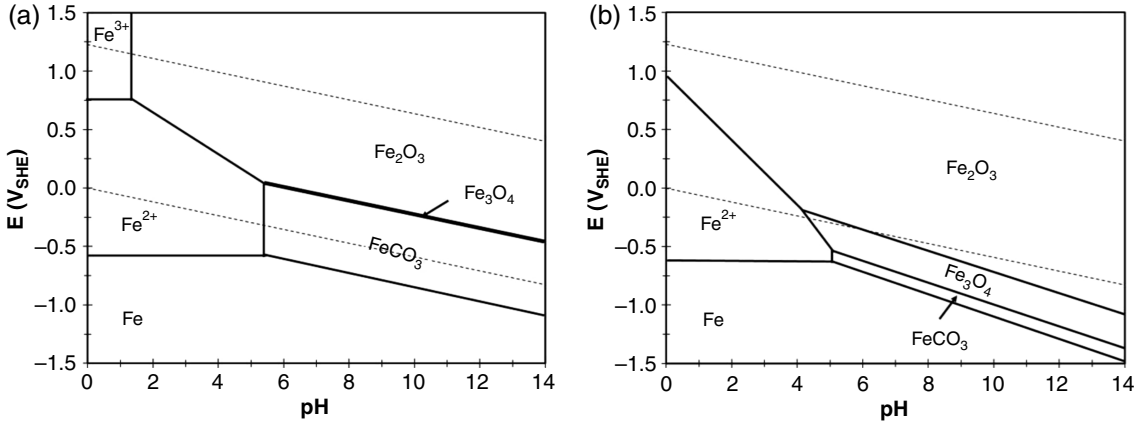

FIGURE 13. *Pourbaix diagram for Fe-CO_2-H_2O system (a) at 80°C and (b) 200°C, 1 bar CO_2 at 25°C.*

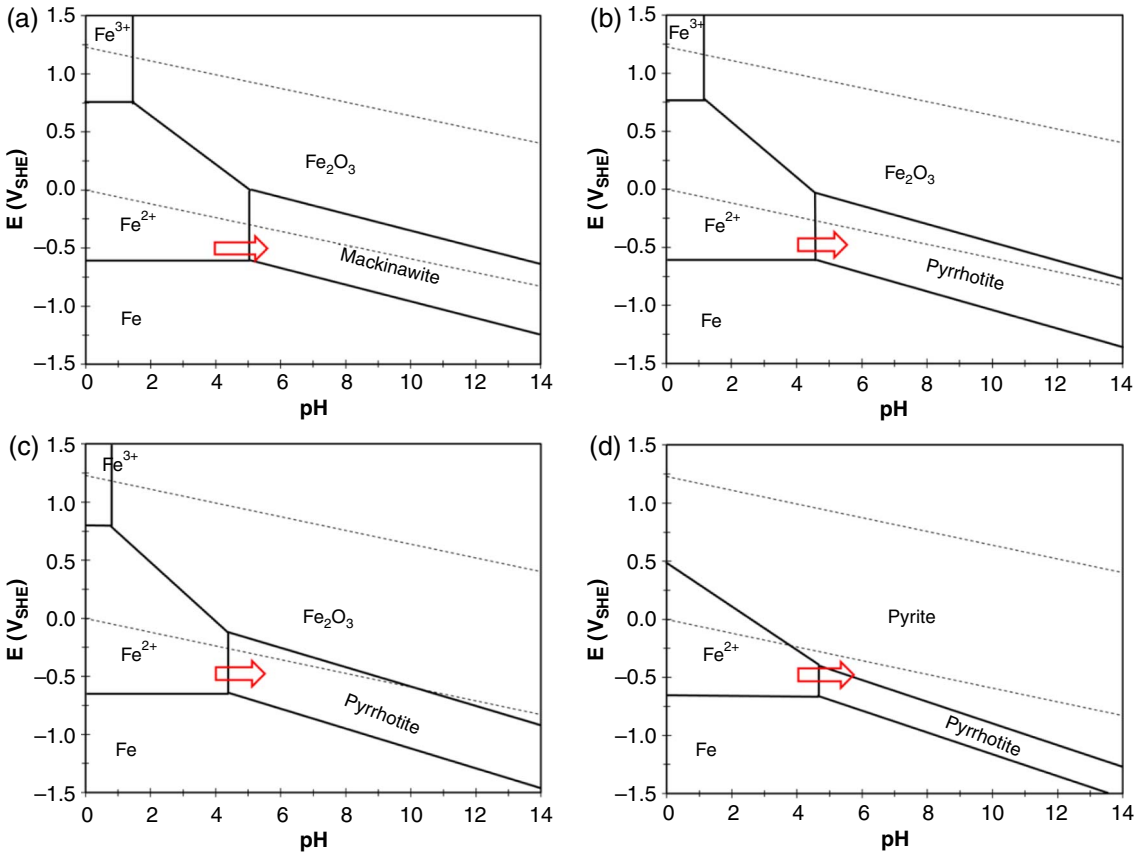

FIGURE 14. *Pourbaix diagram for Fe-H_2S-H_2O system, (a) 80°C, mackinawite, (b) 120°C, pyrrhotite (troilite), (c) 160°C, pyrrhotite, and (d) 200°C, pyrite/pyrrhotite, other input parameters are in Table 4.*

was assumed to be the same as under final conditions. At the experimental temperature pH_2S is also unknown, in addition to the five unknowns mentioned above, but the extra Equation (16) can be used. The calculation results are summarized in Table 4.

Compared with the initial conditions, the final pH values all drifted from 4.00 to above 5.40, which represent conditions increasingly favorable for iron sulfide formation. These parameters are used to generate Pourbaix diagrams as shown in Figure 14. The red arrow represents the pH shifting and the likely potential range (around –500 mV_{SHE}).

The Pourbaix diagrams provide useful information to understand the experimental results. Different polymorphs and related phases of iron sulfides were identified at the different temperatures tested. Fe_3O_4 and mackinawite were always observed after short exposure times, inferring that they always formed first. However, according to the Pourbaix diagrams in H_2S environments, pyrite and pyrrhotite should be more stable than iron oxides and mackinawite, which act as precursors for the transformation reactions.[25] However, pyrrhotite and pyrite were only observed at 160°C and 200°C. This could be explained considering that the transformation kinetics are accelerated at higher temperatures. Particularly at 200°C, the "pH shift" arrow crosses the equilibrium line between pyrrhotite and pyrite, indicating a possible iron sulfide transformation between pyrrhotite and pyrite, which is in good agreement with the XRD data (Figure 8).

CONCLUSIONS

❖ A water chemistry model for a closed system containing H_2S was developed and checked for validity at high temperatures.
❖ Sour corrosion experiments were conducted successfully at 80°C, 120°C, 160°C, and 200°C. Initial corrosion rates increased with increasing temperature. Final corrosion rates, after 4 d of exposure, remained high at between 2 mm/y and 4 mm/y.
❖ Iron sulfide transformation was observed for the first time in high-temperature H_2S corrosion. The inner corrosion product was iron oxide (postulated to be Fe_3O_4), the outer layer was mainly mackinawite, troilite, pyrrhotite, and pyrite at 80°C, 120°C, 160°C, and 200°C, respectively.

ACKNOWLEDGMENTS

The authors would like to express sincere appreciation to the following industrial sponsors for their

financial support and direction: Anadarko, Baker Hughes, BP, Chevron, China National Offshore Oil Corporation, ConocoPhillips, DNV GL, ExxonMobil, M-I SWACO, Occidental Oil Company, Petroleum Institute, PTT, Saudi Aramco, Shell Global Solutions, SINOPEC, TOTAL, TransCanada, WGK.

REFERENCES

1. G. DeBruijin, *Oilfield Rev.* 20, 3 (2008): p. 46-60.
2. H.J. Chen, "High Temperature Corrosion Inhibition Performance of Imidazoline and Amide," CORROSION/2010, paper no. 00035 (San Antonio, TX: NACE, 2010).
3. S.S. Prabha, *Eur. Chem. Bull.* 3, 3 (2014): p. 300-307.
4. H. Ma, X. Cheng, G. Li, S. Chen, Z. Quan, S. Zhao, L. Niu, *Corros. Sci.* 42, 10 (2000): p. 1669-1683.
5. W. Sun, S. Nesic, S. Papavinasam, "Kinetics of Iron Sulfide and Mixed Iron Sulfide/Carbonate Scale Precipitation in CO_2/H_2S Corrosion," CORROSION/2006, paper no. 06644 (San Diego, CA: NACE, 2006).
6. J. Tang, Y. Shao, J. Guo, T. Zhang, G. Meng, F. Wang, *Corros. Sci.* 52, 6 (2010): p. 2050-2058.
7. Y. Zheng, B. Brown, S. Nesic, *Corrosion* 70, 4 (2013): p. 351-365.
8. J. Ning, Y. Zheng, B. Brown, D. Young, S. Nesic, *Corrosion* 71, 8 (2015): p. 945-960.
9. W. Sun, D.V. Pugh, S.N. Smith, S. Ling, J.L. Pacheco, R.J. Franco, "A Parametric Study of Sour Corrosion of Carbon Steel," CORROSION/2010, paper no. 10278 (San Antonio, TX: NACE, 2010).
10. T.A. Ramanarayanam, S.N. Smith, *Corrosion*, 46, 1 (1990): p. 66-74.
11. F. Shi, L. Zhang, J. Yang, M. Lu, J. Ding, H. Li, *Corros. Sci.* 102 (2016): p. 103-113.
12. E.B. Backensto, R.D. Drew, C.C. Stapleford, *Corrosion* 12, 1 (1956): p. 22-32.
13. A.V. Skalunov, G.V. Sretenskaya, G.A. Tsarkov, *Fibre Chem.* 18, 4 (1987): p. 321-325.
14. Y. Qi, H. Luo, S. Zheng, C. Chen, Z. Lv, M. Xiong, *Int. J. Electrochem. Sci.* 9 (2014): p. 2101-2112.
15. Y. Zheng, J. Ning, B. Brown, S. Nesic, *Corrosion* 72, 5 (2016): p. 679-691.
16. T. Tanupabrungsun, D. Young, B. Brown, S. Nesic, "Construction and Verification of Pourbaix Diagrams for CO_2 Corrosion of Mild Steel Valid up to 250°C," CORROSION/2012, paper no. 0001418 (Salt Lake City, UT: NACE, 2012).
17. R. Thodla, F. Gui, K. Evans, C. Joia, I. P. Baptista, "Corrosion Fatigue Performance of Super 13 CR, Duplex 2205 and 2507 for Riser Applications," CORROSION/2010, paper no. 10312 (San Antonio, TX: NACE, 2010).
18. J. Ning, Y. Zheng, B. Brown, D. Young, S. Nesic, "Construction and Verification of Pourbaix Diagrams for Hydrogen Sulfide Corrosion of Mild Steel," CORROSION/2015, paper no. 5507 (Dallas, TX: NACE, 2015).
19. F.E. Jones, G.L. Harris, *J. Res. Natl. Inst. Standards Technol.* 97 (1992): p. 335-340.
20. O.M. Suleimenov, R.E. Krupp, *Geochim. Cosmochim. Acta* 58, 11 (1994): p. 2433-2444.
21. O.M. Suleimenov, T.M. Seward, *Geochim. Cosmochim. Acta* 61, 24 (1997): p. 5187-5198.
22. J. Ning, Y. Zheng, D. Young, B. Brown, S. Nesic, *Corrosion* 70, 4 (2014): p. 375-389.
23. D.D.N. Singh, A. Kumar, *Corrosion* 59, 11 (2003): p. 1029-1036.
24. J. Ning, Y. Zheng, B. Brown, D. Young, S. Nesic, "The Role of Iron Sulfide Polymorphism in Localized H_2S Corrosion of Mild Steel," CORROSION/2016, paper no. 7502 (Vancouver, BC: NACE, 2016).
25. L.G. Benning, R.T. Wilkin, H.L. Barnes, *Chem. Geol.* 167, 1 (2000): p. 25-51.